Energy Storage Materials 27 (2020) 1–8

Contents lists available at ScienceDirect

Energy Storage Materials

journal homepage: www.elsevier.com/locate/ensm

Quasi-solid single Zn-ion conductor with high conductivity enabling dendrite-free Zn metal anode

Yanhui Cui [a], Qinghe Zhao [a], Xiaojun Wu [b], Zijian Wang [a], Runzhi Qin [a], Yuetao Wang [a], Mingqiang Liu [a], Yongli Song [a], Guoyu Qian [a], Zhibo Song [a], Luyi Yang [a,**], Feng Pan [a,*]

[a] School of Advanced Materials, Peking University Shenzhen Graduate School, Shenzhen, 518055, PR China
[b] School of Chemical Biology and Biotechnology, Peking University Shenzhen Graduate School, Shenzhen, 518055, PR China

ARTICLE INFO

Keywords:
Zn anode
Single-ion conductor
Semi-fixed anions
Dendrite
Coulombic efficiency

ABSTRACT

Aqueous Zn-ion batteries (ZIBs) have great potential in the field of large-scale energy storage. However, the dendrite formation on Zn anodes hinders the practical applications of ZIBs. Herein, a zincic perfluorinated sulfonic acid membrane (ZPSAM) is prepared as a quasi-solid single-ion conductor. In this membrane, Zn-ions move along with the negatively charged branched chains which possess a limited degree of freedom, forming fast Zn-ion transport channels. Consequently, ZPSAM exhibits high conductivity (~1.17×10^{-3} S cm^{-1}), enabling stable Zn plating and stripping processes at a current density of 2 mA cm^{-2} over 2000 cycles. In addition, due to the confined anion matrix in the membrane, dendrite formation and side reaction are both effectively suppressed. Finally, by applying the electrolyte in both aqueous super-capacitor and Zn-ion batteries, significantly improved cycling performance can be achieved. This work demonstrates a promising solution for the practical use of Zn metal anode in neutral aqueous media, and thus benefits the development of low-cost, high-performance aqueous energy storage devices.

1. Introduction

Recently years, lithium-ion batteries as energy storage devices are developed and gradually applied in various areas of the human life [1–5]. Due to the limited lithium resource and potential safety issues, various energy storage systems are investigated to replace the lithium-ion batteries, i.e. aqueous Zn-ion batteries (ZIBs) [6–9]. In ZIBs, metal Zn is used as anode due to its unique feature of safety, nontoxicity, stable redox potential in aqueous solution (−0.763 V versus standard hydrogen electrode), and a relative high capacity density of 5855 mAh cm^{-3} (820 mAh g^{-1}) [10]. However, the formation of zinc dendrite and by-products (such as $Zn_4(OH)_6SO_4{\cdot}nH_2O$, ZnO, etc.) during cycling in $ZnSO_4$ electrolyte leads to low coulombic efficiency (CE) and poor cycle life of ZIBs [11]. To resolve these issues, many strategies have been proposed. For example, applying $CaCO_3$ and SiO_2 coating layer to modify electrolyte flux on surface of Zn anode [12], introducing porous active carbon layer and rGO layer [13,14], and all these works show relieving effects on Zn dendrite formation. Other works show the benefiting effects of both relieving the Zn dendrite formation and suppressing the side reaction and/or byproduct formation, i.e. coating a zincophilic protective layer [15], adding additives [16,17], using metal-organic framework (MOF) host [18], replacing $ZnSO_4$ with $Zn(CF_3SO_3)_2$ [19], using a highly concentrated zincic salt [20]. Among the reported work, a MOF with fixed anions as quasi solid electrolyte can obviously affect the Zn plating morphology and reduce the side reactions, showing a promising perspective [21]. However, the fragile feature of MOF electrolyte as well as the low conductivity (2.1×10^{-4} S cm^{-1}) make it impractical for large-scale application.

Herein, a flexible zincic perfluorinated sulfonic acid membrane (ZPSAM) with semi-fixed anion framework is developed as a quasi-solid single Zn-ion electrolyte in ZIBs. The negatively charged branches in the polymer possesses a limited degree of freedom, which allows fast ion transfer within the membrane (forming fast Zn-ion transport channels) [22]. As a result, excellent ionic conductivity (~1.17×10^{-3} S cm^{-1}) can be achieved, leading to a reduced Zn plating/stripping polarization. Zn plating/stripping processes with ultra-low polarization voltage of ~55 mV is achieved under a high current of 2 mA cm^{-2}. Due to the confined anion matrix, the concentration gradient on the electrode surface is

* Corresponding author.
** Corresponding author.
E-mail addresses: yangly@pkusz.edu.cn (L. Yang), panfeng@pkusz.edu.cn (F. Pan).

https://doi.org/10.1016/j.ensm.2020.01.003
Received 2 October 2019; Received in revised form 28 November 2019; Accepted 2 January 2020
Available online 7 January 2020

minimized, which suppresses the formation of Zn dendrite. Moreover, because the absence of SO_4^{2-} inhibits the formation of $Zn_4(OH)_6SO_4{\cdot}nH_2O$, the accumulation of OH^- after the initial hydrogen evolution reaction (HER) process will increase pH value and in turn restrains the subsequent HER process, leading to suppressed side reaction and enhanced coulombic efficiency. In addition, when the ZPSAM is used as electrolyte in an aqueous ultrahigh capacitance porous carbon activated carbon (UCAC/Zn) and VS_2/Zn Zn-ion cells respectively, a good cycling performance can be achieved, verifying the benefiting effect of ZPSAM in aqueous Zn-ion cell.

2. Experimental

2.1. Materials

The perfluorinated sulfonic acid membranes (PSAM) (Nafion, DuPont, HP Membrane, 20 μm, tensile strength 38–41 MPa) and perfluorinated sulfonic acid solution (5 wt% Nafion D520 solution) were purchased from Shanghai Hesen Electric co., LTD. The zinc acetate, sulfuric acid (98%), ammonium vanadate, ammonia, thioacetamide, hydrogen peroxide (30%) and ultrahigh capacitance porous carbon activated carbon (UCAC) were purchased from Aladdin reagents website. N-methyl-2-pyrrolidone (NMP) and carbon black were purchased from Taiyuan Yingze LZY battery sales department. All the reagents were used as received.

2.2. Zincic perfluorinated sulfonic acid membrane preparation

The PSAM were cut into disks with 20 mm diameter before activation as described in previous references. [23,24] Typically, the activation process was proceeded as follows. The disks were orderly stewed 1 h at 80 in 3% H_2O_2 solution, deionized water, 1 mol L^{-1} H_2SO_4 and deionized water respectively. Subsequently, the activated disks were immersed into 500 mL 1 mol L^{-1} zinc acetate solution to replace the protons in $–SO_3H$ with Zn^{2+}. To remove the generated acetate acid, metallic zinc was added into the zinc acetate solution. The reaction lasted 24 h. Finally, the disks were washed with deionized water three times and immersed in deionized water for further used.

2.3. VS_2 preparation

The VS_2 was synthesized by hydrothermal method as reference [25]. Typically, 0.351 g NH_4VO_3, 3 mL ammonia and 45 mL H_2O were mixed into solution, and then 1.7 g thioacetamide was added. After stirred for 1 h at room temperature, the mixture solution was transferred into a 100 mL autoclave and hydrothermal 12 h at 180 °C. Then the black product was collected and washed by water and ethanol. Finally, the product is dried at 60 °C in vacuum for further used.

2.4. Cell assembles

The Nafion D520 solution was evaporated into solid product, and further dissolved in N-Methylpyrrolidone (NMP) to form 10 wt % solution at 80 °C. The UCAC, Nafion and carbon black were mixed in a ratio of 5:4:1 to form a slurry. Then the slurry was coated on titanium foil. Subsequently the foil was transferred into hot oven and dry 24 h at 80 °C. The UCAC on foil was about 1 mg cm^{-2}. Then the foil was rolled by a roller press. Further the foil was coated a Nafion layer. Subsequently, the foil was cut into disks with diameter 10 mm, and activated at 80 °C orderly stewed 1 h in 3% H_2O_2 solution, deionized water, 1 mol L^{-1} H_2SO_4 and deionized water. After that, the electrodes were immersed in 1 mol L^{-1} zinc acetate for ion exchange. Finally, the electrodes were washed with deionized water three times and immersed in deionized water for further used.

The VS_2, acetylene black and polyvinylidene fluoride (PVDF) were mixed uniformly into slurry using NMP in a ratio of 7:2:1. Then the slurry was coated on Ti foil and dried in 80 °C hot oven for 24 h. Subsequently, the foil was rolled by a roller press and cut into disks with diameter 10 mm. The active material loading was about 2 mg cm^{-2}. Before used, the disks were immerged 2 mol L^{-1} $ZnSO_4$ 12 h.

The Zn/Zn symmetric cells were assembled using Zn plates with diameter of 10 mm and thickness of 0.5 mm. The water saturated ZPSAM membranes processed in above section were used as electrolyte and separator directly. And in the contrast cells, the dust-free paper (55% cellulose + 45% polyester) and 2 mol L^{-1} $ZnSO_4$ were used as separator and electrolyte respectively. The assembling of UCAC/Zn or VS_2/Zn cells was similar with the Zn/Zn symmetric cells, except replacing one Zn anode with UCAC or VS_2 cathode respectively. The Ti/Zn asymmetry cells were also similar with the Zn/Zn symmetric cells, except replacing one Zn anode with Ti foil. The cells used for linear sweep voltammetry (LSV) measurement also were similar with the Zn/Zn symmetric cells, except replacing one Zn anode with stainless steel.

2.5. Characterizations

Powder X-ray diffraction (XRD) patterns of Zinc anodes were recorded by a Bruker D8 Advance diffractometer using Cu K_α ($\lambda = 1.541$ Å). Scanning electron microscopy (SEM) images of these membrane cross section and Zn plating morphology were obtained from a Zeiss Supra 55 scanning electron microscope. The element mappings were gotten from an Oxford AZtec energy dispersive spectrometer which was equipped with scanning electron microscope. Electrochemical impedance spectroscopy (EIS), ion transference number, and linear sweep voltammetry (LSV) measurements were performed on a Solartron Analytical electrochemical workstation. Before ion transference number test, the Zn/Zn symmetry battery was re-tested with 72 h. The cycling performance of active carbon/Zn cells and Zn plating/stripping with ZPSAM and $ZnSO_4$ electrolyte were tested by Neware battery test system. The conductivity of ZPSAM electrolyte was measured by EIS method as follows: The water saturated ZPSAM electrolyte was placed in the middle of two stainless steel electrode as shown in Fig. S1, and then the EIS dates were collected on a Solartron Analytical electrochemical workstation. The frequency and voltage amplitude were 10^5–1 Hz and 5 mV respectively. Here, the thickness of ZPSAM is ~0.0023 cm (l), effective area of ZPSAM electrolyte is ~2.0096 cm^2 (S), and resistance of the ZPSAM electrolyte is R. The conductivity (σ) calculated using the equation of $\sigma = l/(R \times S)$.

3. Results and discussions

3.1. Material characterization

The schematic diagram of single Zn^{2+} electrolyte preparation is shown in Fig. 1a. The protons of $–SO_3H$ groups in PSAM are substituted by Zn^{2+} spontaneously to form a structure of two $–SO_3^-$ groups combining with one Zn^{2+}, and generated CH_3COOH (weak acid) will react with Zn powder to form new $Zn(CH_3COO)_2$. Thus, this cyclic reaction process guarantees the complete substitution between protons and Zn^{2+}. The optical photograph of the prepared ZPSAM is shown in Fig. 1b.

To confirm whether the ion exchange in ZPSAM is successful, the cross-sectional SEM image and corresponding energy dispersive spectrometer (EDS) elemental mapping of Zn in ZPSAM were characterized (Fig. 2a–b), which shows that the Zn element distributes uniformly in the cross-section of ZPSAM. Since $Zn(CH_3COO)_2$ is used for ion exchange in PSAM, Fourier transform infrared (FTIR) spectrometry was employed to confirm whether the CH_3COO^- anion resides in the ZPSAM. No characteristic peaks of the symmetry and asymmetry stretch of $–CO_2–$ (Fig. S2) are observed in Fig. 2c, indicating the absence of CH_3COO^- in the ZPSAM after the Zn^{2+} exchange. Therefore, the ion exchange only exists between the protons and the added Zn^{2+}. The linear sweep voltammetry result (Fig. 2d) shows that the ZPSAM electrolyte remains stable up to ~ 2.2 V vs Zn/Zn^{2+}, which is high enough for almost all aqueous Zn battery systems. As an important aspect for ion-conductors, the ionic

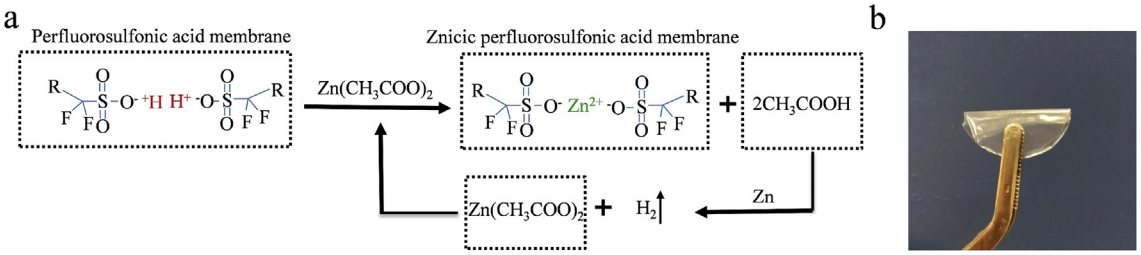

Fig. 1. (a) The schematic diagram of ZPSAM electrolyte preparation; (b) Optical photograph of water saturated ZPSAM electrolyte.

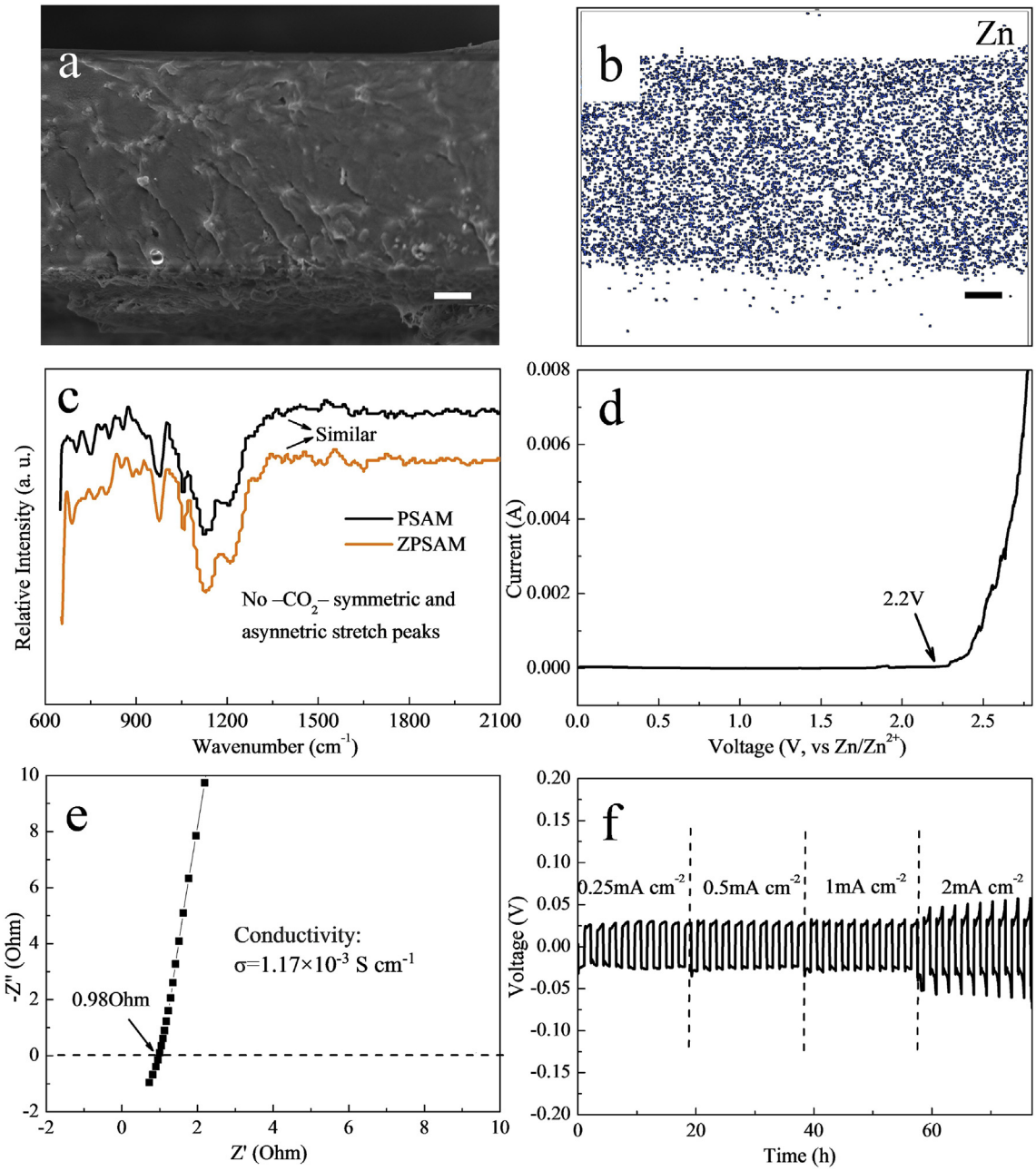

Fig. 2. (a) Cross-sectional SEM image of ZPSAM and the corresponding the Zn mapping (b); (c) FTIR spectra of PSAM and ZPSAM; (d) LSV curve of ZPSAM; (e) EIS plot of ZPSAM; (f) Voltage profiles of Zn/ZPSAM/Zn cell under various current densities. The scale bar in (a) and (b) is 2 μm.

conductivity of ZPSAM is characterized by EIS method. The resistance of the ZPSAM electrolyte is ~0.98 Ohm (R) as shown in Fig. 2e (EIS plot in full-scale is shown in Fig. S3), corresponding to an ion conductivity (σ) of 1.17×10^{-3} S cm^{-1}, which is high enough to enable fast Zn-ion transport.

The Zn/Zn symmetric cell with ZPSAM electrolyte delivers high rate performance shown in Fig. 2f. The polarization voltage is below ~35 mV at current densities from 0.25 mA cm^{-2} to 1 mA cm^{-2}, and even at a high current density of 2 mA cm^{-2}, the polarization voltage is merely ~55 mV.

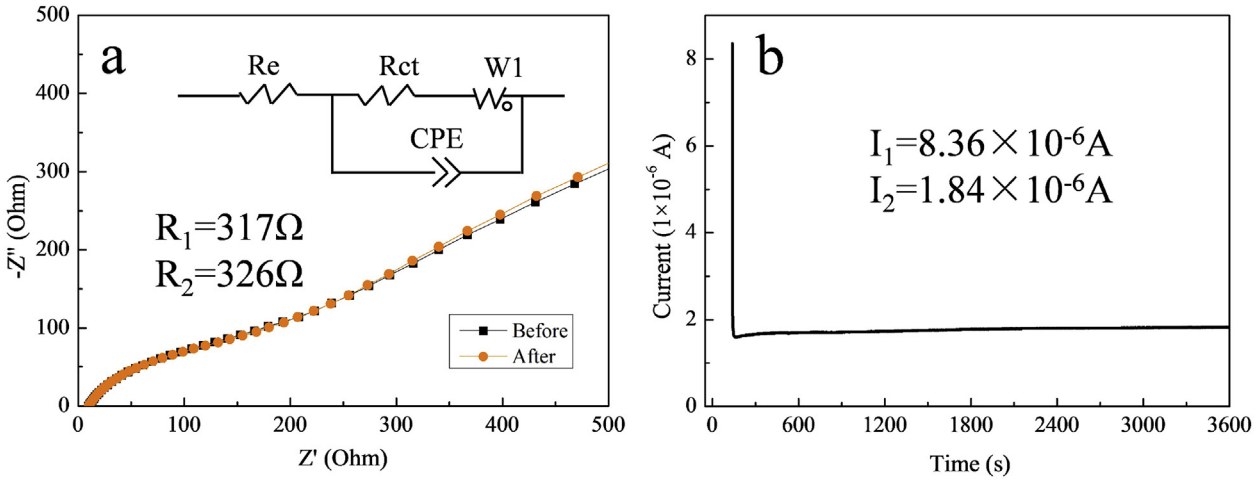

Fig. 3. (a) EIS curves of Zn/Zn symmetry battery with ZPSAM electrolyte before and after potential static 1 h at 20 mV. (b) Current profile of Zn/Zn symmetry battery with ZPSAM electrolyte potential static 1 h at 20 mV.

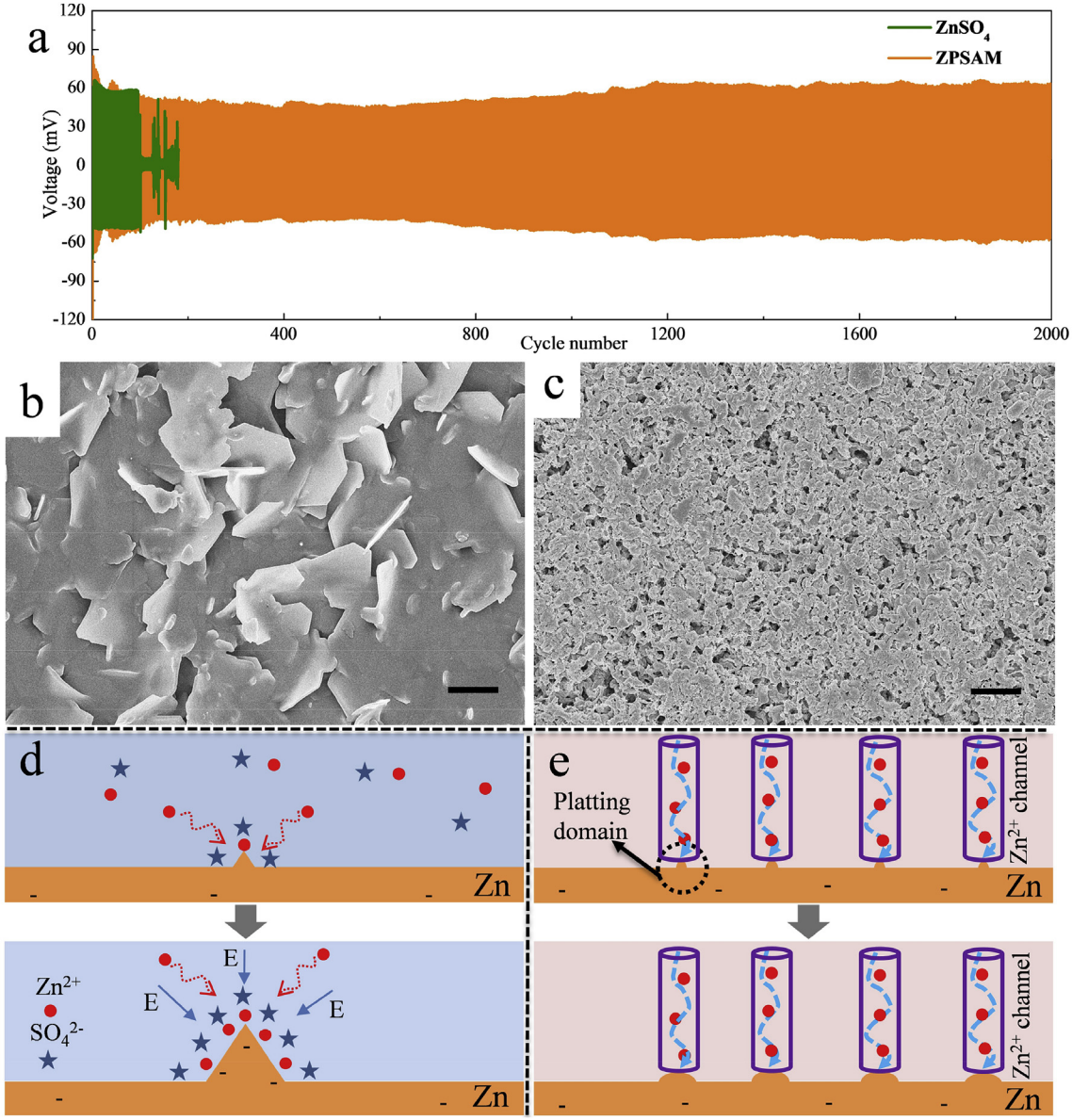

Fig. 4. (a) Cycling performance of Zn/Zn symmetric cells with $ZnSO_4$ electrolyte and ZPSAM electrolyte under different current density 2 mA cm^{-2}, area capacities of all Zn/Zn symmetric cells are 0.5 mAh cm^{-2}; SEM images of Zn plating morphologies at 0.5 mA cm^{-2} 1h: (b) $ZnSO_4$, (c) ZPSAM, and the schematic of Zn plating with (d) $ZnSO_4$ electrolyte and (e) ZPSAM electrolyte. The scale bar is 2 μm.

The Zn ion transference number of ZPSAM electrolyte can be measured and calculated by Evans method (Fig. 3) [26,27]:

$$t_{Zn2+} = I_2(\Delta V - I_1R_1)/I_1(\Delta V - I_2R_2) \quad (1)$$

where, t_{Zn2+} is the Zn ion transference number, ΔV is the applied voltage (V), I_1 is the initial current (A), R_1 is the initial charge transfer resistance (Ohm), I_2 is the final current (A) at a constant voltage with ΔV, R_2 is the final charge transfer resistance (Ohm). Generally speaking, the value of Zn ion transference number is expected to verge on 1 due to the fixed anions in ZPSAM. However, based on the results in Fig. 3, the calculated t_{Zn2+} is ~0.2, which is an abnormal value of transference number for a single ion conductor. Therefore, the ion concentrations are further investigated to rule out the contribution of free anions in total ion transfer, Zn^{2+} concentration in water of ZPSAM after one cycle is as low as $\sim 1 \times 10^{-5}$ mol L^{-1} from ICP-MS results, and the pH value is 8.4. Since the only possible cations in the symmetry battery are Zn^{2+} and H^+, the anions concentration (OH^- and $-SO_3^-$) also should be $\sim 2 \times 10^{-5}$ mol L^{-1}. Therefore, there is few free anions in the ZPSAM electrolyte. We consider that the localized "swing" of semi-fixed anions on long and flexibility branch in the ZPSAM electrolyte is responsible for the abnormal t_{Zn2+}. Nevertheless, ZPSAM electrolyte can still be regarded as a single ion conductor since only Zn^{2+} processes a long-distance diffusion ability inside the ZPSAM electrolyte, while the movement of $-SO_3^-$ containing branch is restricted in a limited area.

Table 1
Performance comparison of galvanostatic Zn stripping/plating in a Zn/Zn symmetrical cell.

Electrolyte	Current density (mA cm^{-2})	Area capacity (mAh cm^{-2})	Operation cycles	Reference
3 mol $ZnSO_4$ + 0.1 mol $MnSO_4$	0.25	0.05	2000	12
8 mol $NaClO_4$ + 0.4 mol $Zn(CF_3SO_3)_2$	2.5	1	300	13
1 mol $ZnSO_4$	1	2	200	14
3 mol $ZnSO_4$ + 0.1 mol $MnSO_4$	3	0.5	500	15
2 mol $ZnSO_4$	20	10	200	18
3 mol $Zn(CF_3SO_3)_2$	0.1	0.1	400	19
1 mol $Zn(TFSI)_2$ + 20 mol LiTFSI	0.2	0.033	510	20
ZnMOF-808 with H_2O	0.1	0.05	350	21
Water saturated ZPSAM	**2**	**0.5**	**2000**	**This work**

3.2. Dendrite depression for Zn metal anode

To study the long-term stability of ZPSAM toward Zn anode, galvanostatic cycling performance of Zn/Zn cells with both $ZnSO_4$ and ZPSAM electrolytes were investigated under different current densities as shown in Fig. 4 and Fig. S4. The cell with ZPSAM electrolyte shows relatively stable voltage profile over 2000 cycles at a current density 2 mA cm^{-2}, exhibiting superior performance compared to the cell using $ZnSO_4$ electrolyte (short circuited with 110 cycles, Fig. 4 a). Similar results are also obtained in current densities of 0.25 and 0.5 mA cm^{-2} as shown in Fig. S4. Moreover, the polarization voltages of Zn/Zn symmetric cells with ZPSAM electrolyte are equivalent with that of cells with $ZnSO_4$ electrolyte. The results of galvanostatic Zn stripping/plating in a Zn/Zn symmetrical cell have been compared with those of recent publications as shown in Table 1. The current density, area capacity and operation cycles of this work show competitive performance in those publications with liquid electrolyte. More importantly, it should be note that the separators used in these work are commonly filter paper, glass fiber or fibre paper whose thicknesses are usually above 150 μm, i.e. the cross section of dust-free paper is shown in Fig. S5, showing a thickness of over 300 μm. Also the thickness of the ZnMOF-808 quasi-solid electrolyte is 300 μm [21]. In this case, the low volumetric energy densities are compromised for Zn ion batteries application. Furthermore, the methods of coating layers on Zn

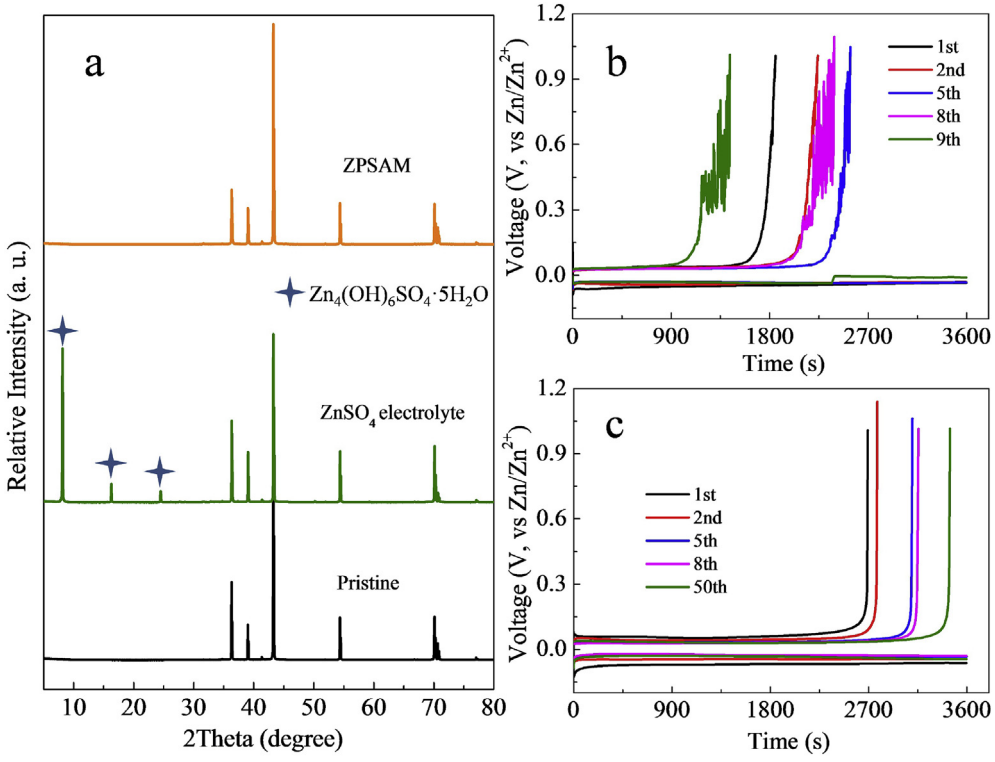

Fig. 5. (a) XRD patterns of pristine Zn, Zn anode after 5 cycles using $ZnSO_4$ and ZPSAM electrolyte at 0.5 mA cm^{-2} and 0.5 mAh cm^{-2}, and voltage vs time profiles of Zn plating/stripping at current of 0.5 mA cm^{-2} using a Zn/Ti foil asymmetry cell with (b) $ZnSO_4$ electrolyte and (c) ZPSAM electrolyte.

surface will aggravate this issue, i.e. the optimal carbon coating layer is about 90 μm [12]. For this work, the thickness of ZPSAM quasi-solid electrolyte is only about 23 μm which is of great importance for developing Zn ion batteries with volumetric energy density.

To compare both the $ZnSO_4$ and ZPSAM electrolytes for Zn plating morphologies, further investigation has been carried out, as shown in Fig. 4b and c and Fig. S6. Some thin small Zn metal slices are observed for Zn plating morphology at 0.25 mA cm^{-2} in $ZnSO_4$ electrolyte (Fig. S6), these slices become larger and obvious as the current density increased up to 0.5 mA cm^{-2} (Fig. 4b). Then the amount of the slices increases, and some bulgy bulks also arise when the current density further increased to 1 and 2 mA cm^{-2} (Figs. S6b and S6c). As the cycling time increased, these slices and bulgy bulks continuously grow and finally result in a short circuit of Zn/Zn symmetric cells. By contrast, the Zn morphology with ZPSAM electrolyte at current of 0.5 mA cm^{-2} shows homogeneous small particle agglomeration, rather than dendrite, as shown in Fig. 4c. Moreover, the size of these small particles uniformly grows with cycling time (Fig. S7). Even at very high current density of 2 mA cm^{-2}, no obvious Zn slices can be seen on the Zn anode with a ZPSAM electrolyte (Fig. S6f).

To reveal the formation mechanism of the two very distinct plating morphologies, $ZnSO_4$ solution was added into the ZPSAM electrolyte and the plating morphologies are shown in Figs. S8a and S8b. Slices-like morphology of Zn plating is also observed, but with much smaller size than that in $ZnSO_4$ electrolyte. Therefore, the formation of Zn dendrite with a $ZnSO_4$ electrolyte is closely related to the free moving anions (SO_4^{2-}). A schematic illustration of Zn plating in a $ZnSO_4$ electrolyte is proposed in Fig. 4d. Similar to the Li dendrite growing [28–30], along with fast electroplating of Zn^{2+} on Zn cusps, a large amount of free moving anions (SO_4^{2-}, coordinated with Zn^{2+}) will accumulate nearby the Zn cusps and result in a space electric field, which drives the Zn^{2+} gathering, accelerates the Zn cusps growth, and finally forms a considerable Zn dendrite. Whereas for a ZPSAM electrolyte, the Zn^{2+} only travels within a confined domain with the nano-wetted contact at the interface between the electrolyte and Zn-metal [31–34] as demonstrated in Fig. 4e, which avoids tip growth effect. As a result, the dendrite formation on Zn anode is inhibited.

3.3. Enhancing effect on CE of Zn anode

The utilization of ZPSAM in ZIB not only depresses the Zn dendrite formation, but also mitigates the side reaction on Zn anode. XRD patterns of different Zn anodes are presented in Fig. 5a. For Zn anode cycled in $ZnSO_4$ electrolyte, 3 obvious peaks located at 8.2°, 16.3° and 24.5° (2theta) arise, belonging to the XRD diffraction pattern of $Zn_4(OH)_6SO_4{\cdot}5H_2O$ (PDF #39–0688). This result indicates a serious side reaction during Zn plating in a $ZnSO_4$ electrolyte:

$$4Zn^{2+} + 6OH^- + SO_4^{2-} + 5H_2O \rightarrow Zn_4(OH)_6SO_4{\cdot}5H_2O \quad (2)$$

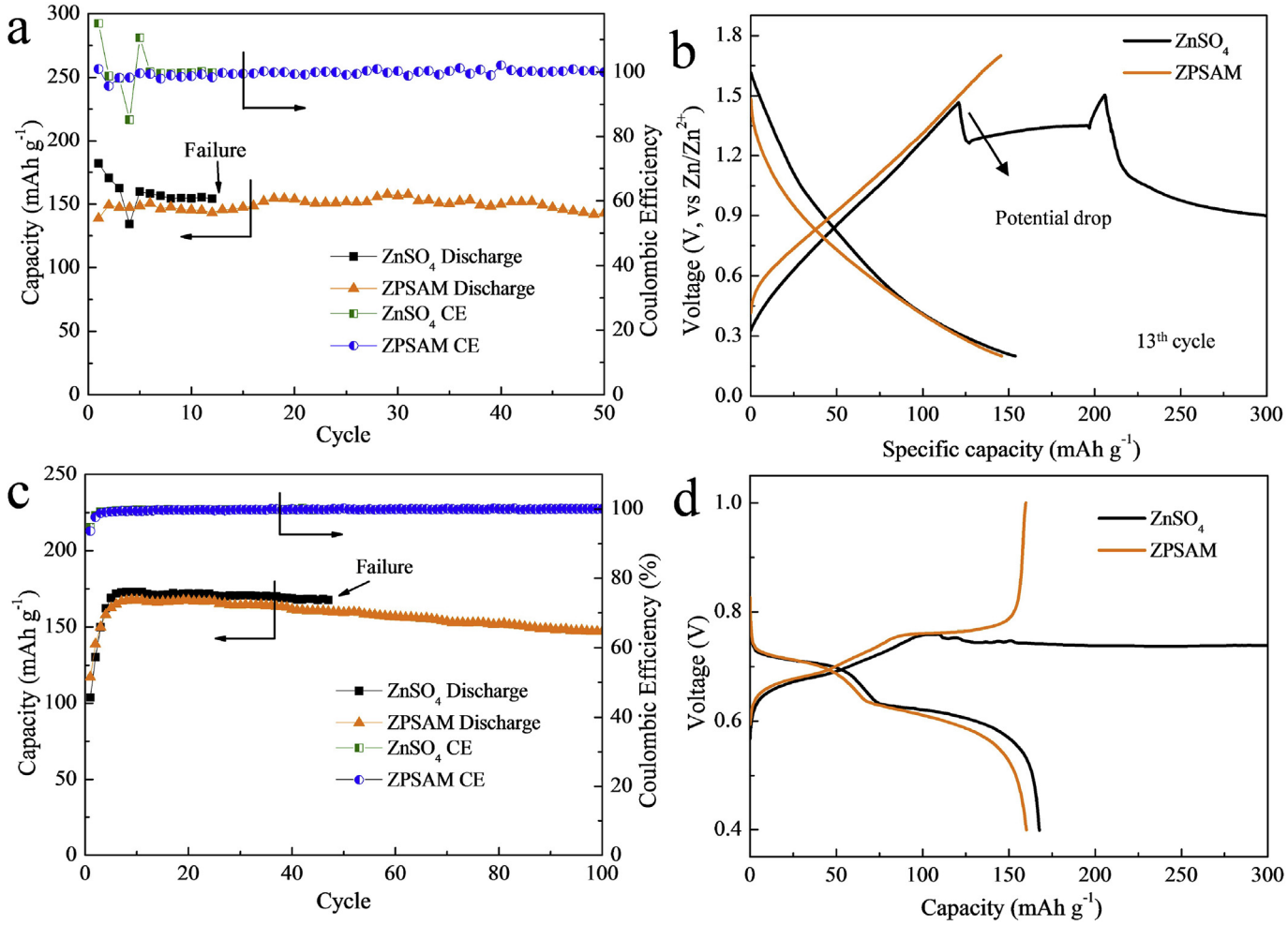

Fig. 6. (a) Cycling performance of UCAC/Zn cells with $ZnSO_4$ electrolyte and ZPSAM electrolyte at 200 mA g^{-1}, (b) 13th discharge/charge curves of UCAC/Zn cells with different electrolyte, (c) Cycling performance of VS_2/Zn batteries with $ZnSO_4$ electrolyte and ZPSAM electrolyte at 200 mA g^{-1}, (d) 44th discharge/charge curves of UCAC/Zn cells with different electrolyte.

which consumes OH^- ions (produced by the hydrogen evolution reaction (HER) process during Zn plating), presses the further increase of pH value in the located area, and then accelerates the subsequent HER process [35]. In addition, the side reaction is further investigated by using Zn/Zn symmetric cells, in which the noncomplete reversible formation of $Zn_4(OH)_6SO_4{\cdot}5H_2O$ is evidenced during Zn cycling shown in Fig. S9. Due to the formation of $Zn_4(OH)_6SO_4{\cdot}5H_2O$, a low CE of Ti/Zn asymmetry cell is obtained, with only ~ 51% and ~66% in the 1st and 8th cycles, respectively (Fig. 5b and Fig. S10). However, XRD patterns of Zn anode cycled with a ZPSAM electrolyte shows no formation of $Zn_4(OH)_6SO_4{\cdot}5H_2O$ byproducts, which is mainly due to the absence of SO_4^{2-}. As a result, OH^- formed during the initial HER process increases the pH value of the Zn/ZPSAM interface and in turn restrains the subsequent HER process (i.e. the pH value of water in ZPSAM significantly increased from 7.1 to 8.4 after 1 cycle at 0.5 mA cm^{-2}. However for 2 M $ZnSO_4$ electrolyte, the pH value only increased from 5.0 to 5.3). Therefore, the side reaction on Zn anode can be effectively suppressed by the utilization of ZPSAM electrolyte. Consequently, a high CE of Ti/Zn asymmetry cell is obtained as shown in Fig. 5c and Fig. S10. The CEs of Ti/Zn asymmetry cell for the 1st and 8th cycles are 75% and 88%, respectively, both of which are higher than that with $ZnSO_4$ electrolyte. In addition, the CE gradually increases and reaches 96% after 50th cycles.

3.4. Performance in Zn-based capacitor

For practical application of the ZPSAM electrolyte, UCAC/Zn cells are assembled and the cycling performance at 200 mA g^{-1} are shown in Fig. 6a. For a UCAC/Zn cell with ZPSAM electrolyte, the discharge capacity is ~138 mAh g^{-1} in the 1st cycle, and increases to 149 mAh g^{-1} in the 2nd cycle due to an activation process. After 50 cycles, the discharge capacity maintains 142 mAh g^{-1}, indicating an outstanding cycling performance, which is much better than that of UCAC/Zn cell with $ZnSO_4$ electrolyte. The cell with $ZnSO_4$ electrolyte fails (Short circuit) only after 12 cycles, as shown in Fig. 6a and b, in which the morphologies of Zn anodes shows severe dendrite formation in Fig. S11a. However, the Zn anode with ZPSAM electrolyte shows relatively smooth surface after cycling (Fig. S11b). In addition, VS_2 has also been synthesized (the XRD pattern is shown in Fig. S12) and used as cathode material in Zn metal batteries, and the electrochemical performances are shown in Fig. 6c and d. In Fig. 6c, the discharge capacities of VS_2 with $ZnSO_4$ electrolyte increase to 173 mAh g^{-1} after activation process and failed at 44th cycle due to the dendrite formation (Fig. S11c). By contrast, in the presence of ZPSAM electrolyte, the discharge capacities also increase to 168 mAh g^{-1} after several cycles' activation and maintain 147 mAh g^{-1} at 100th cycles, corresponding to a relatively smooth Zn anode surface (Fig. S11d). The rate performance test also shows positive result in Fig. S13. It should be noted that, the VS_2 with ZPSAM delivers higher discharge capacity (168 mAh g^{-1}) than the cell using MOF-based electrolyte (151 mAh g^{-1}) due to the higher conductivity of ZPSAM. Due to the imposing restraining effect on Zn dendrite formation and excellent enhancement effect on CE of Zn anodes, the ZPSAM membrane is promising in practical application of ZIB.

4. Conclusions

In summary, a zincic perfluorinated sulfonic acid membrane with semi-fixed anions was designed and prepared as a quasi-solid single Zn-ion conductor. The anions with constrained mobility could form fast Zn-ion transport channels, which leads to impressive high ion conductivity of ZPSAM. Due to the relatively immobilized anion structure in ZPSAM, both dendrite formation on Zn anode and side reactions during cycling are effectively inhibited. Consequently, stable Zn plating and stripping can be achieved under a current density of 2 mA cm^{-2} for over 2000 cycles. In addition, when ZPSAM is operated in an aqueous (UCAC)/Zn and VS_2/Zn cells respectively, excellent cycling performance can be achieved. This work sheds lights on the practical use of Zn metal anode in aqueous media, and thus benefits a lot to the development of low-cost, high-performance aqueous energy storage devices.

Author contribution statement

Yanhui Cui does the main work of the study and prepares the manuscript.

Qinghe Zhao and Xiaojun Wu take part in the design of experiments and capacitor preparation.

Zijian Wang and Runzhi Qin do the XRD characterizations.

Yuetao Wang and Mingqiang Liu do the electrochemical tests.

Songli Song, Guoyu Qian and Zhibo Song take part in the discussion and building of involved mechanism.

Luyi Yang and Feng Pan are as supervisors to the study.

Declaration of competing interest

The authors declare that they have no known competing financial interests or personal relationships that could have appeared to influence the work reported in this paper.

Acknowledgements

This work was financially supported by National Key R&D Program of China (2016YFB0700600), Soft Science Research Project of Guangdong Province (No. 2017B030301013), Shenzhen Science and Technology Research Grant (ZDSYS201707281026184), and China Postdoctoral Science Foundation (2019M650296).

Appendix A. Supplementary data

Supplementary data to this article can be found online at https://doi.org/10.1016/j.ensm.2020.01.003.

References

[1] G. Zubi, R. Dufo-López, M. Carvalho, G. Pasaoglu, The lithium-ion battery: state of the art and future perspectives, Renew. Sustain. Energy Rev. 89 (2018) 292–308, https://doi.org/10.1016/j.rser.2018.03.002.

[2] Y. Cui, X. Wu, J. Wu, J. Zeng, A.P. Baker, F. Lu, X. Liang, J. Ouyang, J. Huang, X. Liu, Z. Li, X. Zhang, An interlayer with architecture that limits polysulfides shuttle to give a stable performance Li-S battery, Energy Storage Mater 9 (2017) 1–10, https://doi.org/10.1016/j.ensm.2017.06.007.

[3] R. Wang, G. Qian, T. Liu, M. Li, J. Liu, B. Zhang, W. Zhu, S. Li, W. Zhao, W. Yang, X. Ma, Z. Fu, Y. Liu, J. Yang, L. Jin, Y. Xiao, F. Pan, Tuning Li-enrichment in high-Ni layered oxide cathodes to optimize electrochemical performance for Li-ion battery, Nano Energy 62 (2019) 709–717, https://doi.org/10.1016/j.nanoen.2019.05.089.

[4] G. Qian, X. Liao, Y. Zhu, F. Pan, X. Chen, Y. Yang, Designing flexible lithium-ion batteries by structural engineering, ACS Energy Lett 4 (2019) 690–701, https://doi.org/10.1021/acsenergylett.8b02496.

[5] Y. Cui, Q. Zhang, J. Wu, X. Liang, A.P. Baker, D. Qu, H. Zhang, H. Zhang, X. Zhang, Developing porous carbon with dihydrogen phosphate groups as sulfur host for high performance lithium sulfur batteries, J. Power Sources 378 (2018) 40–47, https://doi.org/10.1016/j.jpowsour.2017.12.027.

[6] A. Konarov, N. Voronina, J.H. Jo, Z. Bakenov, Y.K. Sun, S.T. Myung, Present and future perspective on electrode materials for rechargeable zinc-ion batteries, ACS Energy Lett 3 (2018) 2620–2640, https://doi.org/10.1021/acsenergylett.8b01552.

[7] D. Yang, H. Tan, X. Rui, Y. Yu, Electrode Materials for Rechargeable Zinc-Ion and Zinc-Air Batteries: Current Status and Future Perspectives, Springer Singapore, 2019, https://doi.org/10.1007/s41918-019-00035-5.

[8] H. Li, L. Ma, C. Han, Z. Wang, Z. Liu, Z. Tang, C. Zhi, Advanced rechargeable zinc-based batteries: recent progress and future perspectives, Nano Energy 62 (2019) 550–587, https://doi.org/10.1016/j.nanoen.2019.05.059.

[9] J. Long, J. Gu, Z. Yang, J. Mao, J. Hao, Z. Chen, Z. Guo, Highly porous, low band-gap $Ni_xMn_{3-x}O_4$ ($0.55 \leq x \leq 1.2$) spinel nanoparticles with in situ coated carbon as advanced cathode materials for zinc-ion batteries, J. Mater. Chem. 7 (2019) 17854–17866, https://doi.org/10.1039/C9TA05101E.

[10] M. Song, H. Tan, D. Chao, H.J. Fan, Recent advances in Zn-ion batteries, Adv. Funct. Mater. 28 (2018) 1–27, https://doi.org/10.1002/adfm.201802564.

[11] X. Zeng, J. Hao, Z. Wang, J. Mao, Z. Guo, Recent progress and perspectives on aqueous Zn-based rechargeable batteries with mild aqueous electrolytes, Energy Storage Mater 20 (2019) 410–437, https://doi.org/10.1016/j.ensm.2019.04.022.

[12] L. Kang, M. Cui, F. Jiang, Y. Gao, H. Luo, J. Liu, W. Liang, C. Zhi, Nanoporous CaCO3 coatings enabled uniform Zn stripping/plating for long-life zinc

rechargeable aqueous batteries, Adv. Energy Mater. 8 (2018) 1–8, https://doi.org/10.1002/aenm.201801090.
[13] W. Li, K. Wang, M. Zhou, H. Zhan, S. Cheng, K. Jiang, Advanced low-cost, high-voltage, long-life aqueous hybrid sodium/zinc batteries enabled by a dendrite-free zinc anode and concentrated electrolyte, ACS Appl. Mater. Interfaces 10 (2018) 22059–22066, https://doi.org/10.1021/acsami.8b04085.
[14] C. Shen, X. Li, N. Li, K. Xie, J.G. Wang, X. Liu, B. Wei, Graphene-boosted, high-performance aqueous Zn-ion battery, ACS Appl. Mater. Interfaces 10 (2018) 25446–25453, https://doi.org/10.1021/acsami.8b07781.
[15] M. Liu, L. Yang, H. Liu, A. Amine, Q. Zhao, Y. Song, J. Yang, K. Wang, F. Pan, Artificial solid-electrolyte interface facilitating dendrite-free zinc metal anodes via nanowetting effect, ACS Appl. Mater. Interfaces 11 (2019) 32046–32051, https://doi.org/10.1021/acsami.9b11243.
[16] K.E.K. Sun, T.K.A. Hoang, T.N.L. Doan, Y. Yu, X. Zhu, Y. Tian, P. Chen, Suppression of Dendrite Formation and corrosion on zinc anode of secondary aqueous batteries, ACS Appl. Mater. Interfaces 9 (2017) 9681–9687, https://doi.org/10.1021/acsami.6b16560.
[17] J. Hao, J. Long, B. Li, X. Li, S. Zhang, F. Yang, X. Zeng, Z. Yang, W.K. Pang, Z. Guo, Toward high-performance hybrid Zn-based batteries via deeply understanding their mechanism and using electrolyte additive, Adv. Funct. Mater. 29 (2019) 1903605, https://doi.org/10.1002/adfm.201903605.
[18] Z. Wang, J. Huang, Z. Guo, X. Dong, Y. Liu, Y. Wang, Y. Xia, A metal-organic framework host for highly reversible dendrite-free zinc metal anodes, Joule 3 (2019) 1289–1300, https://doi.org/10.1016/j.joule.2019.02.012.
[19] N. Zhang, F. Cheng, Y. Liu, Q. Zhao, K. Lei, C. Chen, X. Liu, J. Chen, Cation-deficient spinel ZnMn2O4 cathode in Zn(CF3SO3)2 electrolyte for rechargeable aqueous Zn-ion battery, J. Am. Chem. Soc. 138 (2016) 12894–12901, https://doi.org/10.1021/jacs.6b05958.
[20] F. Wang, O. Borodin, T. Gao, X. Fan, W. Sun, F. Han, A. Faraone, J.A. Dura, K. Xu, C. Wang, Highly reversible zinc metal anode for aqueous batteries, Nat. Mater. 17 (2018) 543–549, https://doi.org/10.1038/s41563-018-0063-z.
[21] Z. Wang, J. Hu, L. Han, Z. Wang, H. Wang, Q. Zhao, J. Liu, F. Pan, A MOF-based single-ion Zn^{2+} solid electrolyte leading to dendrite-free rechargeable Zn batteries, Nano Energy 56 (2019) 92–99, https://doi.org/10.1016/j.nanoen.2018.11.038.
[22] O. Diat, G. Gérard, Fuel cells: proton channels, Nat. Mater. 7 (2008) 13, https://doi.org/10.1038/nmat2091.
[23] Y. Cui, Y. Liu, J. Wu, F. Zhang, A.P. Baker, M. Lavorgna, Q. Wu, Q. Tang, J. Lu, Z. Xiao, X. Liu, Porous silicon-aluminium oxide particles functionalized with acid moieties: an innovative filler for enhanced Nafion-based membranes of direct methanol fuel cell, J. Power Sources 403 (2018) 118–126, https://doi.org/10.1016/j.jpowsour.2018.09.090.
[24] Y. Cui, A.P. Baker, X. Xu, Y. Xiang, L. Wang, M. Lavorgna, J. Wu, Enhancement of Nafion based membranes for direct methanol fuel cell applications through the inclusion of ammonium-X zeolite fillers, J. Power Sources 294 (2015) 369–376, https://doi.org/10.1016/j.jpowsour.2015.06.078.
[25] P. He, M. Yan, G. Zhang, R. Sun, L. Chen, Q. An, L. Mai, Layered VS_2 nanosheet-based aqueous Zn ion battery cathode, Adv. Energy Mater. 7 (2017) 1601920, https://doi.org/10.1002/aenm.201601920.
[26] Y. Feng, R. Tan, Y. Zhao, R. Gao, L. Yang, J. Yang, H. Li, G. Zhou, H. Chen, F. Pan, Insight into fast ion migration kinetics of a new hybrid single Li-ion conductor based on aluminate complexes for solid-state Li-ion batteries, Nanoscale 10 (2018) 5975–5984, https://doi.org/10.1039/c8nr00573g.
[27] V. Fleury, J.N. Chazalviel, M. Rosso, B. Sapoval, Role of the anions in the growth speed of fractal electrodeposits, J. Electroanal. Chem. Interfacial Electrochem. 290 (1990) 249–255, https://doi.org/10.1016/0022-0728(90)87434-L.
[28] J. Evans, C.A. Vincent, P.G. Bruce, Electrochemical measurement of transference numbers in polymer electrolytes, Polymer 28 (1987) 2324–2328, https://doi.org/10.1016/0032-3861(87)90394-6.
[29] J.N. Chazalviel, Electrochemical aspects of the generation of ramified metallic electrodeposits, Phys. Rev. A 42 (1990) 7355–7367, https://doi.org/10.1103/PhysRevA.42.7355.
[30] J. Xiang, L. Yang, L. Yuan, K. Yuan, Y. Zhang, Y. Huang, J. Lin, F. Pan, Y. Huang, Alkali-metal anodes: from lab to market, Joule 3 (2019) 1–30, https://doi.org/10.1016/j.joule.2019.07.027.
[31] Z. Wang, R. Tan, H. Wang, L. Yang, J. Hu, H. Chen, F. Pan, A metal–organic-framework-based electrolyte with nanowetted interfaces for high-energy-density solid-state lithium battery, Adv. Mater. 30 (2018) 1–7, https://doi.org/10.1002/adma.201704436.
[32] Z. Wang, Z. Wang, L. Yang, Y. Song, L. Han, K. Yang, H. Chen, F. Pan, Boosting interfacial Li + transport with a MOF-based ionic conductor for soli-state batteries, Nano Energy 49 (2018) 580–587, https://doi.org/10.1016/j.nanoen.2018.04.076.
[33] K. Wang, L. Yang, Z. Wang, Y. Zhao, Z. Wang, L. Han, Y. Song, F. Pan, Enhanced lithium dendrite suppressing capability enabled by a solid-like electrolyte with different-sized nanoparticles, Chem. Commun. 54 (2018) 13060–13063, https://doi.org/10.1039/c8cc07476c.
[34] L. Han, Z. Wang, D. Kong, L. Yang, K. Yang, Z. Wang, F. Pan, An ordered mesoporous silica framework based electrolyte with nanowetted interfaces for solid-state lithium batteries, J. Mater. Chem. A. 6 (2018) 21280–21286, https://doi.org/10.1039/C8TA08875F.
[35] B. Lee, H.R. Seo, H.R. Lee, C.S. Yoon, J.H. Kim, K.Y. Chung, B.W. Cho, S.H. Oh, Critical role of pH evolution of electrolyte in the reaction mechanism for rechargeable zinc batteries, ChemSusChem 9 (2016) 2948–2956, https://doi.org/10.1002/cssc.201600702.